TRANSVERSE WALL OSCILLATION IMPACT ON VORTEX POPULATIONS IN TURBULENT PIPE FLOW WITH DRAG REDUCTION

Daniel Coxe

Yulia Peet SEMTE

School for Engineering of Matter, Transport and Energy (SEMTE)
Arizona State University
501 E Tyler Mall, Tempe AZ 85281
dcoxe@asu.edu

SEMTE
Arizona State University
ypeet@asu.edu

Ronald Adrian

SEMTE Arizona State University rjadrian@asu.edu

ABSTRACT

The present study investigates the influence of a transverse wall oscillation on the distributions of vortex types and the number density of vortices in a turbulent pipe flow at a moderate Reynolds number ($Re_{\tau} = 720$). Transverse wall oscillations in a current parameter regime yield 23% skin friction drag reduction. To identify connected vortex regions in the flow, an image processing procedure based on an analysis of the swirling strength fields in over 1000 temporal realizations is developed. The results show significant changes to the statistics of the vortex populations within the Stokes' layer of the flow created by wall oscillation. These changes result in a suppression of formation of radially oriented vortices in a walloscillated case, not only in the Stokes' layer, but all through the buffer and the log layer of the flow. This suppression might be associated with a reduced turbulent momentum transfer to the wall in the wall-oscillated case that results in drag reduction.

INTRODUCTION

Since the work of Jung *et al.* (1992), the reduction of skin friction drag by wall oscillations transverse to the mean flow in channels and pipes has been studied extensively (Ricco *et al.*, 2021; Leschziner, 2020). The body of evidence supports a widely held view that suppression of the near-wall turbulent regeneration cycle of near-wall quasi-streamwise vortices results in suppression of turbulent ejections and, consequently, reduction of the mean velocity gradient near the wall (Ricco *et al.*, 2021). More broadly, the Stokes' layer disrupts the near-wall turbulence cycle (Leschziner, 2020).

Above the near-wall layer wall turbulence is largely governed by organization and regeneration of hairpin vortices (Adrian, 2007). Suppression of ejections from the near-wall layer supposedly affects the structure, strength and orientation of these hairpins. It has been hypothesized that the rate of production of hairpin packets by auto-generation (Zhou *et al.*, 1999) is reduced by the weakening of the ejections from the near-wall layer (Kim *et al.*, 2008). This effect further contributes to drag reduction.

While a reduction in strength of ejections and sweeps in wall-oscillated flows has been previously documented via

a statistical analysis of the shear-stress distributions (Yakeno et al., 2014), it is unclear whether there is a visible effect of these important statistical changes on the organization and orientation of the vortex populations in such flows. Visualizations have been previously made regarding vortical structures in wall-oscillated flows (see, e.g. Coxe et al. (2019); Kempaiah et al. (2020)). However, no work currently exists to quantify the effect of wall oscillation on the alignment, orientation and organization of the vortex structures in a statistical sense. We remark that a similar study in canonical (non wall-oscillated) wall-bounded flows has been attempted by Wu & Christensen (2006); Gao et al. (2011).

The current paper presents a study on the distribution of the vortex angles under the influence of transverse wall oscillations in a pipe flow. It aims to determine how the near-wall and the log-layer vortices are manipulated, through the change in their probable orientation angles, by the wall oscillation at a moderate Reynolds number ($Re_{\tau} = 720$). The probability density functions (pdfs) of the vortex orientations and the number density of certain types of vortices throughout the domain are compared with and without the wall oscillations in a turbulent pipe flow.

PROBLEM SETUP

Direct numerical simulations (DNS) were carried out at a moderate Reynolds numbers, $Re_{\tau} = u_{\tau}R/v = 720$ (R is the pipe radius, $u_{\tau} = \sqrt{\tau_w/\rho}$ is the friction velocity, τ_w is the mean wall shear stress, ρ is the density, and v is the kinematic viscosity of the fluid) using an open-source spectral element solver Nek5000 (Fischer *et al.*, 2015). More details about the simulations can be found in Coxe *et al.* (2019); Peet *et al.* (2023). Wall oscillations are introduced via specifying a temporally varying azimuthal wall velocity as:

$$u_{\theta}(x, r = R, \theta, t) = W \sin\left(\frac{2\pi t}{T}\right),$$
 (1)

with wall oscillation parameters (in wall units) chosen to be $T^+=100$, $W^+=10$ (T^+ is the period, and W^+ is the velocity amplitude of the wall oscillations), which were shown to

correspond to near-optimum values for controlling near-wall turbulence (Quadrio & Ricco, 2004). The result of this wall oscillation is 14% increase in a bulk flow rate of the pipe at $Re_{\tau} = 720$, which translates into 23% reduction of skin friction coefficient (Peet *et al.*, 2023).

VORTEX ANALYSIS METHOD

To characterize the vortex populations in the flow, the swirling strength (λ_{ci}) is calculated for each temporal snapshot. The swirling strength λ_{ci} is determined as the magnitude of the imaginary part of the complex conjugate pair (Chakraborty *et al.*, 2005) of the eigenvalues of the fluctuating turbulent velocity gradient tensor $\nabla \mathbf{u}''$, \mathbf{u}'' denoting the triply decomposed fluctuating field (Hussain & Reynolds, 1970) to remove the periodically sheared Stokes' layer.

A vortex point is identified when a threshold of the swirling strength is met. This threshold is given by $\lambda_{ci} > 1.25 \times \partial U_e/\partial l$, where $\partial U_e/\partial l$ is introduced as a scaling parameter based on a characteristic velocity gradient (Gao *et al.*, 2011). This scaling was shown to provide a good collapse of the swirling strength across different data sets while being less sensitive to a measurement noise in a study of Gao *et al.* (2011). Characteristic velocity gradient, $\partial U_e/\partial l$, is defined as the mean of the tensor invariants of the velocity fluctuation gradient tensor $(\nabla \mathbf{u}'')$ when swirling is present: $\partial U_e/\partial l = (\|\langle I_1|\lambda_{ci}>0\rangle_{x,\theta,t}\|+\sqrt{\langle I_2|\lambda_{ci}>0\rangle_{x,\theta,t}}+\sqrt{\langle I_3|\lambda_{ci}>0\rangle_{x,\theta,t}}/3$, where $I_1=Tr(\nabla \mathbf{u}'')$, $I_2=\frac{1}{2}\left((Tr(\nabla \mathbf{u}''))^2-\left((\nabla \mathbf{u}'')^2\right)\right)$, $I_3=Det(\nabla \mathbf{u}'')$, and $\langle \cdot |\lambda_{ci}>0\rangle$ denotes a conditional averaging over the regions which have non-zero swirling strength. Utilizing the above threshold, a binary field $\Xi(\mathbf{x})$ is constructed:

$$\Xi(\mathbf{x}) = \begin{cases} 1, & \lambda_{ci} > 1.25 \times \partial U_e / \partial l \\ 0, & \text{otherwise} \end{cases}$$
 (2)

This field distinguishes the points which can be considered as a part of a vortex (with $\Xi(\mathbf{x})=1$) from the vortex-free points (with $\Xi(\mathbf{x})=0$).

Next, an image segmentation algorithm (Virtanen, 2020) is applied to the binary field $\Xi(\mathbf{x})$, sampled at streamwise-azimuthal planes at specified radial locations, to determine the connected regions of vortices. A connected region of vortex points is identified as a vortex (Ω) if its size exceeds a threshold of $r^+ = \sqrt{A_{vort}/(2\pi)} > 10$ (Gao *et al.*, 2011), where A_{vort} is the area of the connected region at a corresponding streamwise-azimuthal plane. For each grid point within the identified vortex, the eigenvector (Λ_r) associated with the real eigenvalue (λ_r) is calculated, and the mean value for each vortex, $\bar{\Lambda}_r$, is obtained as the average across the vortex volume. To determine the orientation of the vortex in a three-dimensional space, its average eigenvector, $\bar{\Lambda}_r$, is projected onto the three cross-sectional planes, and the corresponding inclination angles in each plane are defined accordingly as:

$$\phi_{x,-r} = \arctan\left(\frac{-\sigma_{\bar{\Lambda}_r}\bar{\Lambda}_r \cdot \hat{e}_r}{\sigma_{\bar{\Lambda}_r}\bar{\Lambda}_r \cdot \hat{e}_x}\right)$$
(3)

$$\phi_{\theta,x} = \arctan\left(\frac{\sigma_{\bar{\Lambda}_r}\bar{\Lambda}_r \cdot \hat{e}_x}{\sigma_{\bar{\Lambda}_r}\bar{\Lambda}_r \cdot \hat{e}_\theta}\right) \tag{4}$$

$$\phi_{-r,\theta} = \arctan\left(\frac{\sigma_{\bar{\Lambda}_r}\bar{\Lambda}_r \cdot \hat{e}_{\theta}}{-\sigma_{\bar{\Lambda}_r}\bar{\Lambda}_r \cdot \hat{e}_r}\right),\tag{5}$$

where $\sigma_{\bar{\Lambda}_r} = \mathrm{sign}(\overline{\omega} \cdot \bar{\Lambda}_r)$, with $\overline{\omega}$ being the vorticity vector averaged over the vortex region Ω , and $(\hat{e}_x, \hat{e}_r, \hat{e}_\theta)$ are the unit vectors in the (x, r, θ) coordinate directions, respectively. Multiplication by the vorticity vector $\overline{\omega}$ in the calculation of $\sigma_{\bar{\Lambda}_r}$ is adopted to remove the ambiguity related to the fact that a mathematical definition of the eigenvector is sign invariant. This allows us to distinguish between positively and negatively oriented vortices in our analysis.

Lastly, to quantify the statistical effect of wall oscillation on vortex populations, we compute the probability density function of the distribution of the vortex angles at a specified radial coordinate as:

$$P[\phi_{i,j}](r) = \lim_{w \to 0} \frac{\overline{N}(r)|_{\phi_{i,j}}}{w \sum_{\phi_{i,j}} \overline{N}(r)|_{\phi_{i,j}}},\tag{6}$$

where w is the bin width in degrees, and $\overline{N}(r)|_{\phi_{i,j}}$ is the number density of vortices with the angle $\phi'_{i,j}$ lying within the interval $\phi'_{i,j} \in [\phi_{i,j} - w/2, \phi_{i,j} + w/2]$, computed as an average over a streamwise-azimuthal cross-sectional plane across all temporal realizations at a given radial coordinate:

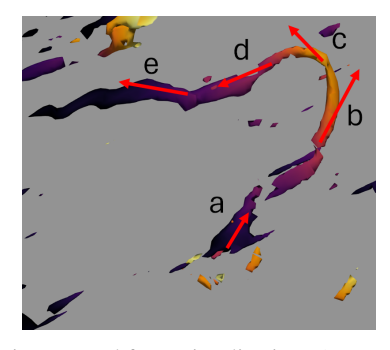
$$\overline{N}(r)|_{\phi_{i,j}} = \frac{1}{2\pi r L N_{snap}} \sum_{k=1}^{N_{snap}} N_k(r)|_{\phi_{i,j}}, \tag{7}$$

where L is the length of the pipe, and $N_k(r)|_{\phi_{i,j}}$ is the total number of vortices with the corresponding condition on their angle, identified at a given radial location at each temporal snapshot. To calculate the probability distribution in equation (6) numerically, we consider a bin width of $w=5^\circ$. A total of $N_{snap}=1024$ snapshots separated by $\Delta t^+=3.125$ were used in the statistical analysis.

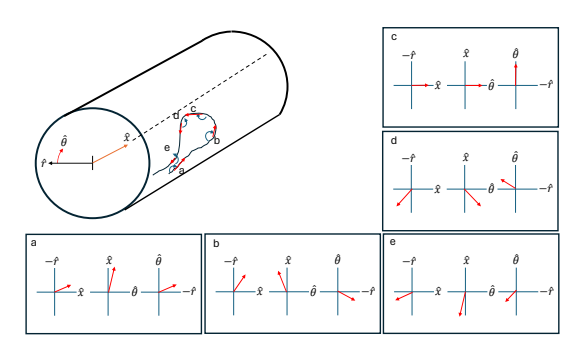
INTERPRETATION OF VORTEX ANGLES

To provide an intuitive interpretation of the vortex angles defined in equations (3)-(5), we invoke a well-established hairpin vortex model of wall turbulence (Zhou et al., 1999; Adrian, 2007). Figure 1a shows such a hairpin vortex as captured in the visualizations (of a non-oscillated pipe flow in the current DNS), Figure 1b offers a conceptual schematic of such a hairpin, together with the expected vortex orientation angles along the different parts of the hairpin structure, while Figure 1c demonstrates a view of a hairpin in a radial-azimuthal plane. Hairpin vortices are typically formed by a pair of counter-rotating quasi-streamwise vortices (hairpin legs) that come close together and induce a sufficient updraft to start lifting themselves up (forming the hairpin necks) that eventually join to form a hairpin head (Zhou et al., 1999; Adrian, 2007). The schematic in Figure 1b distinguishes between the hairpin legs (labeled as 'a' and 'e'), necks ('b' and 'd'), and head ('c'), and illustrates the typical angles that can be expected for each of the identified parts (taking into account their orientation, which, e.g., is positive for the right leg 'a' and negative for the left leg 'e'). We remark that, due to its well-defined formation mechanism, this "traditional" hairpin results in a unique, positive in the current coordinate system, orientation of its head (aligned with the positive θ direction and corresponding to $\phi_{-r,\theta} = +90^{\circ}$, see panel (c) in Figure 1b), which is frequently referred to as a "prograde" vortex (Wu & Christensen, 2006). The oppositely-oriented, "retrograde" vortices (corresponding to $\phi_{-r,\theta} = -90^{\circ}$), are possible as well, but are typically less frequent in wall-bounded flows (Wu & Christensen, 2006).

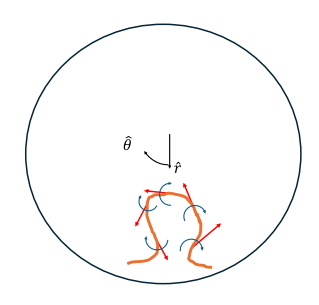
13th International Symposium on Turbulence and Shear Flow Phenomena (TSFP13) Montreal, Canada, June 25–28, 2024



(a) A hairpin captured from visualizations (current DNS of a non-oscillated case).



(b) A schematic of a hairpin and the associated angles of the projected eigenvector at the locations 'a'-'e'.



(c) Hairpin vortex in a radial-azimuthal plane (head and necks). Perspective is looking down the pipe in the direction of flow: clockwise rotation of swirling is positive.

Figure 1: Conceptual model of a turbulent hairpin vortex. Associated eigenvectors are shown as red arrows, and an associated orientation of swirling is shown as blue curved arrows. The schematic corresponds to a traditional (prograde) hairpin.

RESULTS

Figures 2 a,c,e show the distribution of the vortex angles in a streamwise-radial (x,-r) plane plotted at selected wall-normal locations given by $y^+=R^+-r^+$. The peak in the distribution $\phi_{x,-r}$ is centered around 11° at $y^+=25$, 11° at $y^+=50$, 16° at $y^+=100$, and 17° at $y^+=200$ for the uncontrolled (no wall oscillation) case. These angles are consistent with the growth angle of coherent vortex packets observed in the literature (Adrian, 2007; Bai *et al.*, 2024). The shift, as a result of wall oscillation, is subtle. Figures 2 a,c,e

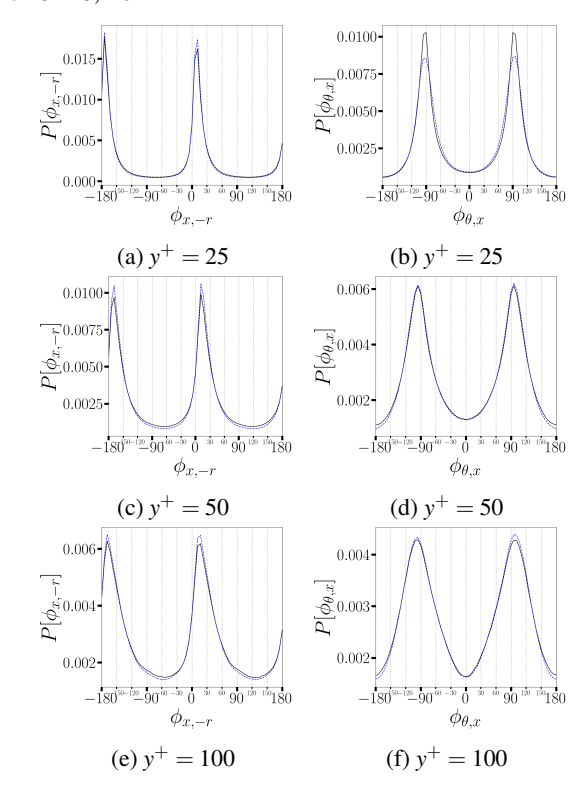


Figure 2: Distribution of the vortex angles as projected onto: Left panel (a,c,e), a streamwise-radial (x,-r) plane; Right panel (b,d,f), an azimuthal-streamwise (θ,x) plane, at different wall-normal locations. Black lines correspond to no wall oscillation, and blue lines are with wall oscillation.

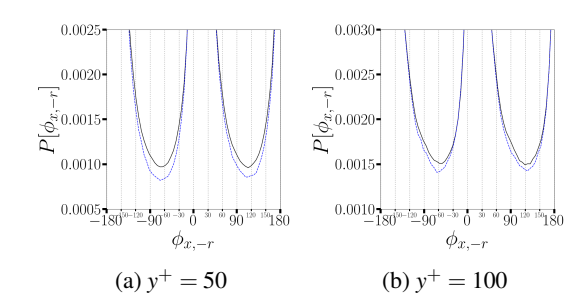


Figure 3: Zoomed-in view through the 'troughs' of the probability density functions of $\phi_{x,-r}$.

show an increased probability of streamwise-oriented vortices $(\phi_{x,-r} \approx 0^{\circ})$, while inhibiting the nearly up-right orientations $(\phi_{x,-r} \approx \pm 90^{\circ})$ in the buffer and the log layer of the flow $(y^{+} \le 100)$, which can be better viewed in a zoomed-in frame in Figure 3. These angles correspond to the up-right oriented hairpin necks (panels (b),(d) in Figure 1b). A decreased likelihood of the necks formation potentially signifies weaker or distorted quasi-streamwise vortices that are unable to produce a sufficient amount of the mutually induced flow leading to a lift-up, an important process in the hairpin formation and auto-generation (Zhou et al., 1996, 1999). Since fewer of the quasi-streamwise vortices lift up, more of them stay parallel to the wall, thus increasing the probability of $\phi_{x,-r} \approx 0^{\circ}$ angles in oscillated flow. Above the log-layer, no significant effect of the wall oscillation on the distribution of vortices in (x, -r)plane is observed.

We next consider the distribution of the vortex angles in an azimuthal-streamwise (θ, x) plane in Figures 2 b,d,f. In

this plane, an angle of $\phi_{\theta,x}=\pm 90^\circ$ corresponds to the vortices aligned with the streamwise direction and pointing downstream and upstream respectively. Figures 2 b,d,f show that most of the impact of the wall oscillation is contained within the buffer layer $(y^+ = 25)$. At this wall normal location, the Stokes' layer can still have a distinct impact on vortices since the Stokes' layer extends to approximately $y^+ = 25$ in the current flow regime (Coxe et al., 2022). At this location, the wall oscillation acts to diffuse the probability density function. A slightly higher probability of $\phi_{\theta,x}$ angles between -90° and $+90^{\circ},$ commensurate with a slight decrease in probability of encountering purely streamwise-oriented vortices ($\phi_{\theta,x} = \pm 90^{\circ}$) in this plane is a manifestation of the sloshing effect of wall oscillations: due to an induced azimuthal motion in the Stokes' layer, the quasi-streamwise vortices are skewed left and right and spend less time oriented straight. One can see that this trend does not persist above $y^+ = 25$, where a direct influence of the Stokes' layer is no longer felt. Instead, in the log layer, one can note a decreased probability of $\phi_{\theta,x} = \pm 180^{\circ}$ (corresponding to the "retrograde" azimuthal vortices, the opposite of the panel (c) in Figure 1b) and an increased probability of $\phi_{\theta,x}=\pm 90^\circ$ (streamwise-aligned structures), especially in the top part of the log layer ($y^+ = 100$). A decrease in the probability of the retrograde vortices in the upper log layer with wall oscillation is interesting. Wu & Christensen (2006) observed that retrograde vortices are the most prominent at the outer edge of the log layer, often nesting near clusters of prograde vortices. Their reduction by wall oscillation might indirectly point to a weakening of the prograde vortex clusters, however this phenomenon needs to be further investigated. We remark that the effects above the log layer are subtle.

Lastly, we present the distribution of the vortex angles in a radial-azimuthal $(-r, \theta)$ plane in Figure 4. To understand the vortex organization in this plane, the reader is referred to Figure 1c. From a hairpin vortex model perspective, whose shape can be described by a "horseshoe" type structure in the $(-r, \theta)$ plane, the $\phi_{-r,\theta}$ angle characterizes the vortices that constitute the head and necks of a hairpin. The first observation from Figure 4 is a significantly higher probability of vortices with $\phi_{-r,\theta} = 90^{\circ}$ (corresponding to prograde vortices, see Figure 1) than $\phi_{-r,\theta} = -90^{\circ}$ (retrograde vortices) at wall-normal locations above $y^+ = 25$. This is consistent with the observations of Wu & Christensen (2006) who reported a higher number of prograde versus retrograde vortices in turbulent channel flows and boundary layers. While there is a clear dip in the pdf distributions at $\phi_{-r,\theta} = -90^{\circ}$ at these locations, the two peaks at slightly lower and slightly higher (negative) angles are observed: these angles are associated with the lower right shoulder (peak between $-90^{\circ} < \phi_{-r,\theta} < 0^{\circ}$) and lower left shoulder $(-180^{\circ} < \phi_{-r,\theta} < -90^{\circ})$ of prograde hairpins (see Figure 1c), which are abundant in both uncontrolled and controlled flows. We now turn to describe the effect of wall oscillations. These effects are the most significant within the buffer layer in the $(-r, \theta)$ plane (Figures 4a,b). This wall-normal location $(y^+ = 25)$ reveals the signature of the quasi-streamwise vortices (QSVs); the hairpin necks and heads typically form higher away from the wall. Without wall oscillation, the QSVs are oriented predominantly in the streamwise direction, while their inclination may exhibit small random fluctuations in both radial and azimuthal directions. This leads to a random exploration of the entire $(-r, \theta)$ space with equal probability, exactly what is reflected in the pdfs in Figures 4a,b. With wall oscillation, transverse motions in the Stokes' layer periodically tilt the QSVs to the left and to the right, resulting in the occur-

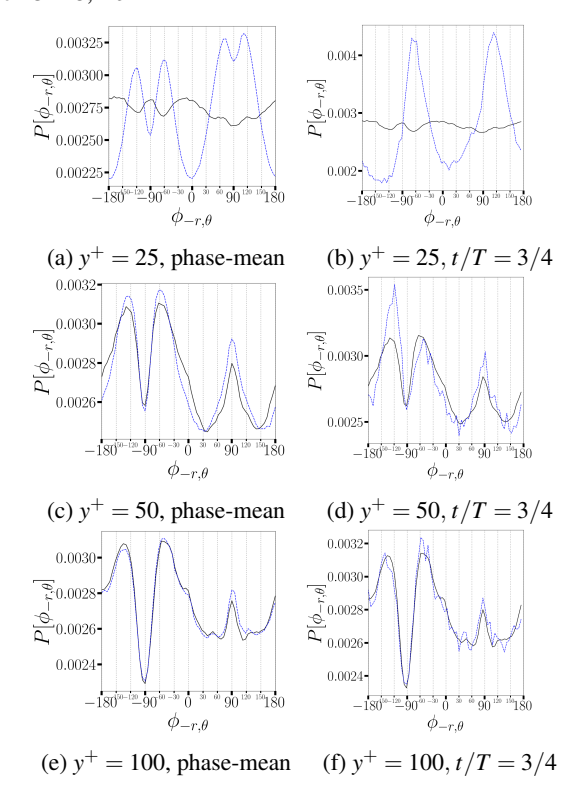
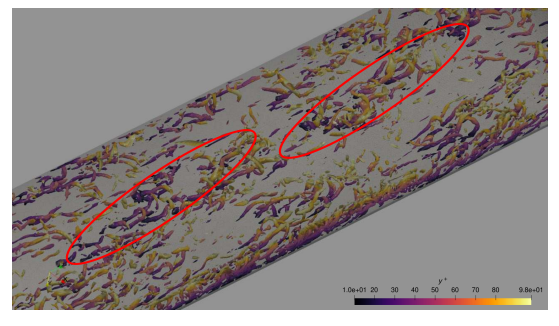
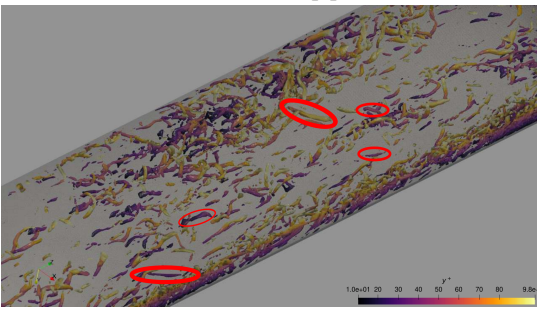


Figure 4: Distribution of the vortex angles as projected onto a radial-azimuthal $(-r,\theta)$ plane at different wall-normal locations. Black lines correspond to no wall oscillation, and blue lines are with wall oscillation. Left panel (a,c,e), phase-mean data; Right panel (b,d,f), constant phase of t/T=3/4.

rence of preferential $\phi_{-r,\theta}$ angles (likely affected by the wall oscillation amplitude). To further demonstrate the effect of vortex tilting by wall oscillation, the right panel of Figure 4 (b,d,f) plots the probability density function computed during a specific phase of the oscillation cycle, namely at t/T = 3/4, when the wall moves counter-clockwise and the wall velocity reaches its maximum ($u_{\theta} = -W$), see equation (1). Figure 4b shows a nearly symmetric distribution, enhancing a distinct band of $\phi_{-r,\theta}$ angles with 180° periodicity (due to the opposite orientation of the pairs of the counter-rotating QSVs). What is interesting is that the probability of the vortices oriented radially (or almost radially) in both Figures 4a and 4b is significantly reduced by wall oscillation. This reduction was already seen in the (x, -r) plane, but is more pronounced in the $(-r, \theta)$ plane. This effect is still felt within the log layer of the flow $(y^+ = 50)$, where a reduction in $\phi_{-r,\theta}$ angles close to 0° and close to $\pm 180^{\circ}$ is visible. This impediment of radially oriented vortices reduces the amount of radial transfer of streamwise momentum via ejections and sweeps and lowers the turbulent burst activity. Both these effects potentially contribute to drag reduction. This suppression of the up-right necks is commensurate with an augmentation of the tilted shoulders (see Figure 1c). However, as Figure 4d shows, this augmentation is not symmetric in a time-dependent frame: at a given phase of the wall oscillation, only one shoulder in the pair of the counterrotating vortices in enhanced. This is consistent with the hypothesis that, when the wall motion is, e.g., counterclockwise, the vortex with the counterclockwise rotation (the left shoulder with $-180^{\circ} < \phi_{-r,\theta} < -90^{\circ}$, see Figures 1c and 4d) is enhanced, while the other is weakened; this is reversed during the second half of the cycle (Coxe et al., 2019). This asymmetry results in an abundance of "skewed", or "one-legged"



(a) Non-oscillated pipe flow.



(b) Oscillated pipe flow.

Figure 5: Contours of the normalized swirling strength, $\lambda_{ci}/(\partial U_e/\partial l)=2.5$ (twice the threshold for vortex identification) colored by wall-normal coordinate.

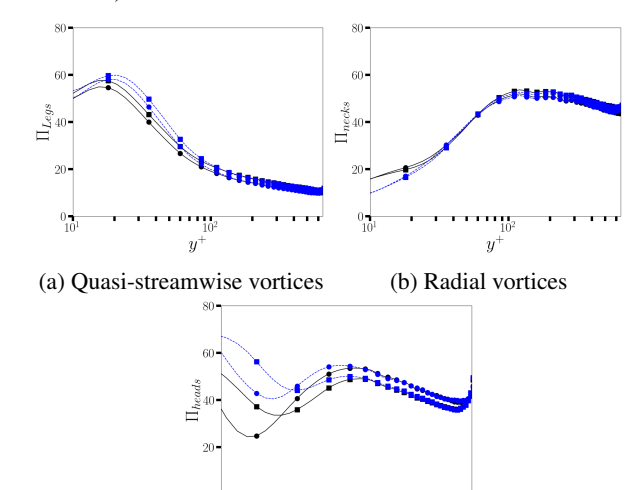
hairpins, which are not as effective in reproduction. The distributions of $\phi_{-r,\theta}$ are not significantly affected at the top of the log layer and above (Figure 4 c,f), showing that the most significant modification of turbulence structure due to wall oscillations is confined to the buffer and the log layer, commensurate with our previous observations (Peet *et al.*, 2023).

To further illustrate the effect of wall oscillation on the vortical structures, we present a three-dimensional visualization of the normalized swirling strength, $\lambda_{ci}/(\partial U_e/\partial l)$, taken at the same oscillation phase of t/T = 3/4 as in the previous analysis in Figure 5. The red ovals highlight, in Figure 5a (non-oscillated case), hairpin packets. The reader's attention is brought to this because such a phenomenon is not readily apparent in the wall-oscillated case (Figure 5b). The signature of one can be seen near the left wall in the oscillated case. However, the characteristic succession of larger hairpins is not readily visible. It is conceivable however, that this might be a local feature of a given realization. It is also easy to notice that there is a large number of tilted hairpins in the oscillated case, some of them are highlighted by red ovals in Figure 5b. Since the wall motion at the presented phase (t/T = 3/4) is counterclockwise, the vortices are predominantly tilted to the right, as expected. It can also be seen that such tilted vortices mostly appear as one-legged, and the number of perfectly formed hairpins is significantly reduced in the oscillated case as compared to the non-oscillated case.

The last portion of our analysis provides a vortex count for the vortices with different orientations in both flows. To this end, and informed by previously shown distributions, we classify each vortex into one of the three categories, depending on its orientation in each of the three principle planes:

1. Streamwise-oriented vortices (legs):

$$\begin{split} &\Omega_{x,+} \in \left\{ (-20^{\circ} \leq \phi_{x,-r} \leq 20^{\circ}) \cap (70^{\circ} < \phi_{\theta,x} < 110^{\circ}) \right\} \\ &\Omega_{x,-} \in \left\{ (160^{\circ} < \phi_{x,-r} \cup \phi_{x,-r} > 160^{\circ}) \cap (-70^{\circ} > \phi_{\theta,x} > -110^{\circ}) \right\} \end{split}$$



(c) Azimuthal vortices

Figure 6: Number density of vortices counted in the flow. Black lines correspond to no wall oscillation, and blue lines are with oscillation. The squares indicate the negative orientation, and the circles indicate the positive orientation of the vortices.

2. Radially-oriented vortices (necks):

$$\Omega_{r,+} \in \left\{ (20^{\circ} < \phi_{x,-r} < 160^{\circ}) \cap -45 < \phi_{-r,\theta} < 45 \right\}$$

$$\Omega_{r,-} \in \left\{ (-160^{\circ} < \phi_{x,-r} < -20^{\circ}) \cap (-135^{\circ} > \phi_{-r,\theta} \cup \phi_{-r,\theta} > 135^{\circ}) \right\}$$

3. Azimuthally-oriented vortices (heads):

$$\begin{split} &\Omega_{\theta,+} \in \left\{ (-70^\circ < \phi_{\theta,x} < 70^\circ) \cap (45^\circ < \phi_{-r,\theta} < 135^\circ) \right\} \\ &\Omega_{\theta,-} \in \left\{ (-110^\circ > \phi_{\theta,x} \cup \phi_{\theta,x} > 110^\circ) \cap (-135^\circ < \phi_{-r,\theta} < -45^\circ) \right\} \end{split}$$

We note that the above three categories are mutually exclusive, i.e. each vortex is counted only once, thus preserving the total number of vortices in the domain. We further distinguish between the positive (+, clockwise if looking from the inlet down the pipe) orientation, and negative (-, counter-clockwise), refer to Figure 1. The vortex number density in each group, $\Pi(r)|_{\Omega_{i,\pm}} = \overline{N}(r)|_{\Omega_{i,\pm}}$, with $\overline{N}(r)|_{\phi_{i,j}}$ defined by equation (7), is plotted in Figure 6 for positively and negatively oriented "legs", "necks" and "heads", respectively.

The main conclusion from Figure 6 is a mild increase in the number of streamwise oriented vortices accompanied by a decrease in the number of radial vortices, especially in the buffer layer. This observation is consistent with our previous results that showed a reduction in the probability density of the radially-oriented vortices (necks). A lower number of necks persists not only in the buffer layer but also in and above the log layer, consistent with our previous observations. For the azimuthal vortices, as expected, we see more positively oriented, prograde, vortices (hairpin heads) than negatively oriented (retrograde) vortices, above the buffer layer. Close to the wall, the azimuthal vortices do not represent the hairpin heads and are not formed by ejections (which would give them a prograde orientation), but rather by a random reorientation of QSVs, sweep events, or tilting by wall oscillations. Tilting/sloshing effects explain a higher number of azimuthal vortices near the wall in the wall-oscillated case.

DISCUSSION

The probability density distributions of vortex inclination angles show only marginal differences in (x, -r) and (θ, x) planes, while differences are quite significant in $(-r, \theta)$ plane, especially if clipped at a certain phase angle. This is due to the fact that the pdfs in (x, -r) and (θ, x) planes are strongly dominated by streamwise-oriented vortices, showing large peaks at their corresponding orientation angles, so that all other effects are obfuscated. In a transverse plane, to the contrary, the changes related to a tilting and reorientation of vortices due to wall oscillation is strong.

The main effect of wall oscillation on the vortex populations at this Reynolds number is manifested as a reduction in a probability of the radially-oriented vortices, typically associated with the mutual lift-up of closely-positioned QSVs. The steep vortex growth angles in turbulent wall-bounded flows has been linked to the legs of the Π type vortices (de Silva *et al.*, 2016) and the hairpin necks (Adrian, 2007). The reduction of these steep angles in wall-oscillated flows has two important consequences: 1) It reduces turbulent momentum transfer to the wall; 2) It reduces turbulent burst activity that has previously been linked with the formation of new hairpins (Zhou et al., 1999; Adrian, 2007). Both these effects are conducive to drag reduction. Another interesting effect of wall oscillation is a reduction in a probability of retrograde azimuthal vortices in the log layer of the pipe visible in $\phi_{\theta,x}$ distributions (reduction of $\phi_{\theta,x} = \pm 180^{\circ}$ angles). Since retrograde vortices are often found on top of the clusters of prograde vortices (Wu & Christensen, 2006), their reduction should theoretically evidence towards the inhibition of the haiprin packets.

The results of the total vortex count observed for the entire time period of $t^+ \in [0,3200]$ give a direct evidence to the reduction in the number of radially-oriented vortices all throughout the top of the log layer, and especially in the buffer layer. The number of streamwise vortices, however, is slightly increased all through the top of the log layer. This could be either due to a suppression of lift up that consequently leaves more vortices oriented in a predominantly streamwise direction, or tearing of the long vortices by oscillatory motions causing them to appear as multiple vortices. The number of azimuthal vortices, while increased in the Stokes' layer due to sloshing, is essentially unchanged at the top part of the log layer. This is despite an indirect evidence that the hairpin packets must weaken (as judged by the suppression of the necks that should inhibit auto-generation, and by the reduction in retrograde vortices), and a direct evidence of weaker packets from visualizations. This can be explained by the fact that while the oscillated flow may contain more vortices per se, they appear to be more broken, more ill-formed, less coherent, and potentially less capable of inducing organized transfer of energy and momentum towards the wall, which is the cause of drag increase in turbulent flows. Indeed, while the current method counts the number of vortices, it does not differentiate between their size, strength and coherence, and counts all the vortices as equal, as long as their size and strength exceed a certain threshold. Future work will develop the methodologies, which will account for these aspects of vortex organization while analyzing the vortex population statistics.

ACKNOWLEDGEMENTS

This work was supported by NSF CBET-1944568 and NSF CBET-2345157 grants.

REFERENCES

- Adrian, R. J. 2007 Hairpin vortex organization in wall turbulence. *Physics of Fluids* **19** (4).
- Bai, T., Cheng, C. & Fu, L. 2024 Investigation of the inclination angles of wall-attached eddies for streamwise velocity and temperature fields in compressible turbulent channel flows. *Physical Review Fluids* 9 (3), 034611.
- Chakraborty, P., Balachandar, S. & Adrian, R. J. 2005 On the relationships between local vortex identification schemes. *Journal of Fluid Mechanics* **535**, 189–214.
- Coxe, D. J., Peet, Y. T. & Adrian, R. J. 2019 Vorticity statistics and distributions in drag reduced turbulent pipe flow with transverse wall oscillations. In *TSFP Symposium*, 2019.
- Coxe, D. J., Peet, Y. T. & Adrian, R. J. 2022 On Stokes' second problem solutions in cylindrical and Cartesian domains. *Physics of Fluids* **34** (10).
- Fischer, P., Lottes, J., Kerkemeier, S., Marin, O., Heisey, K., Obabko, A., Merzari, E. & Peet, Y. 2015 Nek5000: User's manual. *ANL Technical Report No. ANL/MCS-TM-351*.
- Gao, Q., Ortiz-Duenas, C. & Longmire, E. K. 2011 Analysis of vortex populations in turbulent wall-bounded flows. *Journal* of Fluid Mechanics 678, 87–123.
- Hussain, A. K. M. F. & Reynolds, W. C. 1970 The mechanics of an organized wave in turbulent shear flow. *Journal of Fluid mechanics* **41** (2), 241–258.
- Jung, W.-J., Mangiavacchi, N. & Akhavan, R. 1992 Suppression of turbulence in wall-bounded flows by high-frequency spanwise oscillations. *Phys. Fluids* 4 (8), 1605–1607.
- Kempaiah, K. U., Scarano, F., Elsinga, G. E., Van Oudheusden, B. W. & Bermel, L. 2020 3-dimensional particle image velocimetry based evaluation of turbulent skin-friction reduction by spanwise wall oscillation. *Phys. Fluids* 32 (8).
- Kim, K., Adrian, R. J., Balachandar, S. & Sureshkumar, R. 2008 Dynamics of hairpin vortices and polymer-induced turbulent drag reduction. *PRL* 100 (13), 134504.
- Leschziner, M. A. 2020 Friction-drag reduction by transverse wall motion—a review. *J. Mechanics* **36** (5), 649–663.
- Peet, Y., Coxe, D. & Adrian, R. 2023 Loss of effectiveness of transverse wall oscillations for drag reduction in pipe flows with Reynolds number. In 10th THMT Symp., Rome, Italy.
- Quadrio, M. & Ricco, P. 2004 Critical assessment of turbulent drag reduction through spanwise wall oscillations. *Journal of Fluid Mechanics* **521**, 251–271.
- Ricco, P., Skote, M. & Leschziner, M. A. 2021 A review of turbulent skin-friction drag reduction by near-wall transverse forcing. *Progress in Aerospace Sciences* **123**, 100713.
- de Silva, C. M., Hutchins, N. & Marusic, I. 2016 Uniform momentum zones in turbulent boundary layers. *Journal of Fluid Mechanics* **786**, 309–331.
- Virtanen, et. al. 2020 SciPy 1.0: Fundamental Algorithms for Scientific Computing in Python. *Nat. Methods* **17**, 261–272.
- Wu, Y. & Christensen, K. T. 2006 Population trends of spanwise vortices in wall turbulence. *J. Fluid Mech.* **568**, 55–76.
- Yakeno, A., Hasegawa, Y. & Kasagi, N. 2014 Modification of quasi-streamwise vortical structure in a drag-reduced turbulent channel flow with spanwise wall oscillation. *Physics of Fluids* **26** (8), 085109.
- Zhou, J., Adrian, R. J. & Balachandar, S. 1996 Autogeneration of near-wall vortical structures in channel flow. *Physics of Fluids* 8 (1), 288–290.
- Zhou, J., Adrian, R. J., Balachandar, S. & Kendall, T. M. 1999 Mechanisms for generating coherent packets of hairpin vortices in channel flow. *J. Fluid Mech.* 387, 353–396.